Physics of the Earth and Planetary Interiors 351 (2024) 107195

Contents lists available at ScienceDirect

Physics of the Earth and Planetary Interiors

journal homepage: www.elsevier.com/locate/pepi

A meteorology approach to assess mantle flow induced dynamic topography using object-based image processing methods

Ayodeji Taiwo [a,c,*], H.-P. Bunge [a], G. Craig [b]

[a] Department of Earth and Environmental Sciences, University of Munich, Munich 80333, Germany
[b] Meteorological Institute Munich, Munich 80333, Germany
[c] d-fine GmbH, An der Hauptwache 7, 60313 Frankfurt, Deutschland

ARTICLE INFO

2000 MSC:
0000
1111
PACS:
0000
1111
Keywords:
Dynamic topography
Model assessment
Mantle convection
Meteorology

ABSTRACT

The construction and assessment of model trajectories that link multiple mantle states is essential to constrain poorly known mantle convection parameters. Previously, volumetric approaches have been applied to assess the quality of constructed mantle flow trajectories. However, there is a need to assess these trajectories based on their dynamic topography predictions because mantle convection cannot be directly observed and may be inferred via its surface geological expressions. Typical metrics for assessing dynamic topography suffer from the *double penalty problem* — a prediction that is correct in intensity, size, and timing, but incorrect in location, results in large root-mean-square errors when compared to an observation. Here, we introduce metrics, gleaned from meteorology, that decompose any number of dynamic topography fields into their distinct objects after which the similarity between objects is compared. We find that this object-based approach overcomes double penalty and assesses models in a robust manner by providing the ability to assess separately the quality of match between subsidence and uplift areas. Additionally, the approach allows independent quality assessment of multiple aspects of a dynamic topography field, including amplitude and location of dynamic topography.

1. Introduction

Over the past years, our understanding of the surface expressions of mantle convection has much improved. One such expression is the dynamic topography (Hager et al., 1985) of the Earth, which represents Earth's uplift and subsidence, away from its isostatically compensated state [see (Braun, 2010), for a recent review]. In attempting to compare mantle flow trajectories against the real Earth, it is necessary to assess the fit between an actual geological observable and a mantle flow prediction of the same observable. Recently, dynamic topography has been extensively studied both for the present-day (Hoggard et al., 2016; Richards et al., 2020; Holdt et al., 2022) and the past (Bunge and Glasmacher, 2018; Ghelichkhan et al., 2021). For instance, information on its scale, amplitude and temporal evolution has been gleaned via sediment provenance (Şengör, 2001) and river profile studies (Roberts and White, 2010). The most recent effort to obtain proxy constraints about its temporal evolution is the analysis of hiatus maps (Friedrich et al., 2018; Vibe et al., 2018; Carena et al., 2019; Hayek et al., 2020; Hayek et al., 2021). These observations provide insight into the rapidly evolving nature of geologically recent mantle convection. In other words, they offer a lens into the mantle convection system.

Parallel to this, geodynamicists have made progress in computing mantle flow trajectories for the geological past. To this end, two main computational approaches have been developed. The first, referred to as mantle circulation models (MCMs), starts off with an arbitrarily chosen past state of the mantle and models mantle flow forward in time while assimilating plate motions and subduction histories (Bunge et al., 2002; McNamara and Zhong, 2005). The second is the adjoint method (Bunge et al., 2003; Ismail-Zadeh et al., 2004; Horbach et al., 2014; Ghelichkhan and Bunge, 2016; Price and Davies, 2017) in which a present-day estimate of the mantle state, obtained from seismic tomography (Simmons et al., 2007; Ritsema et al., 2011; French and Romanowicz, 2014) is retrodicted in such a way as to improve the unknown past structure. Because of the chaotic nature of mantle convection (Stewart and Turcotte, 1989), mantle flow is subject to the so-called *butterfly effect* — the trajectories of two identical mantle convection models initialized with slightly different temperature fields diverge exponentially in time until they become uncorrelated as demonstrated by (Bello et al., 2015). This effect seemingly rules out the construction of reliable mantle flow trajectories. However, geodynamicists have learned (Colli et al., 2015;

* Corresponding author.
E-mail address: Ayodeji.Taiwo@d-fine.com (A. Taiwo).

https://doi.org/10.1016/j.pepi.2024.107195
Received 8 August 2023; Received in revised form 23 February 2024; Accepted 10 April 2024
Available online 16 April 2024

Vynnytska and Bunge, 2015; Bocher et al., 2016; Bocher et al., 2018) that by assimilating the horizontal component of the surface velocity field into a mantle model, the butterfly effect can be overcome and robust mantle flow trajectories can be constructed. For the real Earth, these horizontal surface velocity motions are now available through past plate motion reconstructions over a period of at least 230 million years (Myrs) (Müller et al., 2016) and more recently, global plate reconstructions have been developed that extend as far back as 1 billion years (Müller et al., 2022), although with increasing uncertainty back in time. One key source of uncertainties relates to the influence of the reference frame. See (Shephard et al., 2012) which investigates the imapct of choice of reference frames in mantle circulation models.

These developments necessitate an exploration of ways in which mantle models can be compared via their dynamic topography responses. One approach involves qualitative comparisons that visually identify areas of (dis-)agreement on multiple dynamic topography maps (e.g. Colli et al., 2018). A second approach — quantitative gridpoint analyses, such as root-mean-square (rms) errors/amplitudes (e.g. Flament et al., 2013; Forte and Rowley, 2022) and spectral decompositions/correlations (e.g. Davies et al., 2019; Valentine and Davies, 2020) — offers a numerical measure of model performance. It should, however, be noted that in the case of spectral decompositions, the double penalty (see Abstract) only enters if one were to perform spatial comparisons across the various wavelengths of the decomposed field. Additional methods of assessing dynamic topography fields were introduced to geodynamics in (Taiwo et al., 2023) through the use of the Taylor diagram. These approaches, however, suffers from a key drawback that has been explored extensively by meteorologists studying weather models (Baldwin and Kain, 2006; Casati et al., 2008; Wilks, 2011; Jolliffe and Stephenson, 2012), namely: it is often difficult to give a physical interpretation to their numerical output. Also, the results of these measures may differ from, rather than complement, inferences based on a visual examination of the prediction and observation. For instance, it is possible for a predicted dynamic topography field to match observations in terms of timing, intensity and pattern of uplift (or subsidence) but to be wrong in location. An informed visual observation would classify this as a good prediction and separately account for the location error. A gridpoint-based rms quality measure, however, would penalize the prediction and classify it as poor. This is termed the *double penalty problem* (e.g. Anthes, 1983; Mass et al., 2002). By double penalty, it is meant that a prediction which matches an observation in all respects except in location is penalized twice; first at the gridpoints in the prediction that do not overlap the observation, and at those gridpoints in the observation that do not overlap the prediction. It is thus imperative, in the use of dynamic topography as an indicator for mantle convection trajectories, to introduce object-based verification metrics which overcome the double penalty problem.

Though new to geodynamics, object-based verification [see (Gilleland et al., 2009), for a summary] has been routinely performed in meteorology to evaluate forecasts of extratropical and lee cyclones (Smith and Mullen, 1993), sea breezes (Case et al., 2004), as well as deep, moist convection (Fowle and Roebber, 2003). One of the more prominent object-based techniques is the Method for Object-based Diagnostic Evaluation (MODE) (Davis et al., 2006a; Davis et al., 2006b; Davis et al., 2009) applied to precipitation forecasts. The method uses a convolution-thresholding procedure to identify precipitation objects on forecast and observation maps and compares statistics (centroid, grid points, bounding contours, area, total rainfall etc.) for every matched pair of objects, thus allowing one to focus on regions of interest on a map.

In this paper, we link to meteorology and introduce object-based tools for assessment of dynamic topography. To this end, we use a multi-level approach as follows: the first level assesses the ability of the prediction to match objects in the observation (Roebber, 2009). The second level compares the structure, amplitude and location differences among all predicted and observed objects without matching them (Wernli et al., 2008). The final level compares the statistics of matched objects and performs a Procrustes shape analysis (Micheas et al., 2007; Lack et al., 2010) to produce a final score that represents the accuracy of a prediction. Our paper is arranged as follows: Section 1.1 describes the models used in this study. Section 2 outlines the methodology of our study. Here we describe the details of our multi-level approach. In Section 3, we present the results of our study and in Section 4, we discuss the results and draw conclusions.

1.1. Models

Our dynamic topography maps (Fig. 1) are a result of standard incompressible isoviscous, pure internal heating mantle convection simulations (Taiwo et al., 2023) at an internal heating Rayleigh number of 3×10^7 and a radial grid spacing of 22 km and 30 km tangentially at the surface, decreasing to half that value at the CMB. We allow a dynamic mantle model to evolve with a free-slip boundary condition at the surface until it reaches a statistical steady-state at which point model quantities such as the rms velocity field are quasi-steady (see True State of Fig. 1a). This reference field is then perturbed in a manner analogous to seismic tomographic regularizations (Trampert and Spetzler, 2006). Three types of perturbations were introduced namely: radial smoothing (see Radial Smoothing in Fig. 1a), which is a radial averaging (over an interval of 100km above and below each gridpoint) of the reference field; horizontal smoothing (see Horizontal Smoothing in Fig. 1a), which is a spherical harmonic expansion and truncation of the reference field at degree 20; S20RTS smoothing (see S20RTS in Fig. 1a), which is a filtering of the reference field via the resolution operator of seismic model S20RTS (Ritsema et al., 2004; Schuberth et al., 2009). All four models, that is the reference model and the three perturbed models, are allowed to evolve freely without velocity assimilation over a transit time ($\approx$ 150 Myrs), which is the time it takes for material to traverse the mantle depth and is thus a relevant time standard to observe the surface effects of changes in the large scale buoyancy structure of the mantle. Since, as mentioned earlier, velocity assimilation helps alleviate the butterfly effect, thus leading to robust trajectories, we repeat the simulations of the perturbed models and assimilate the surface velocity field of the reference model (i.e. True State).(Table 1)

1.1.1. Dynamic topography calculation

As presented in (Taiwo et al., 2023), we compute dynamic topography from the propagator matrix technique (Richards and Hager, 1984). A spherical harmonic expansion of all necessary quantities is performed and the semi-analytical solutions are presented as sensitivity kernels, $K_l(r)$. These kernels can be interpreted as impulse-response functions which relate dynamic topography to a unit density anomaly of given wavelength and depth throughout the depth of the mantle. Each spherical harmonic coefficient δh_{lm} for surface dynamic topography is computed in the spectral domain by

$$\delta h_{lm} = \int_{R_{CMB}}^{R_{Earth}} \delta\rho_{lm}(r) K_l(r) dr \tag{1}$$

In Eq. (1), r is the radius, R_{Earth} and R_{CMB} are the radii of the Earth at the surface and the CMB, respectively, and $\delta\rho_{lm}$ is the density anomaly of spherical harmonic degree l, and order m. Following (Colli et al., 2018), all density anomalies shallower than 200 km are disregarded during the computation of dynamic topography, as they are related to either the thermal cooling of the oceanic lithosphere or compositional heterogeneity of the continental lithosphere (Lithgow-Bertelloni and Silver, 1998). The final dynamic topography values are obtained by a resummation of the spherical harmonic coefficients computed from Eq. (1) truncated at $\ell_{max} = 20$.

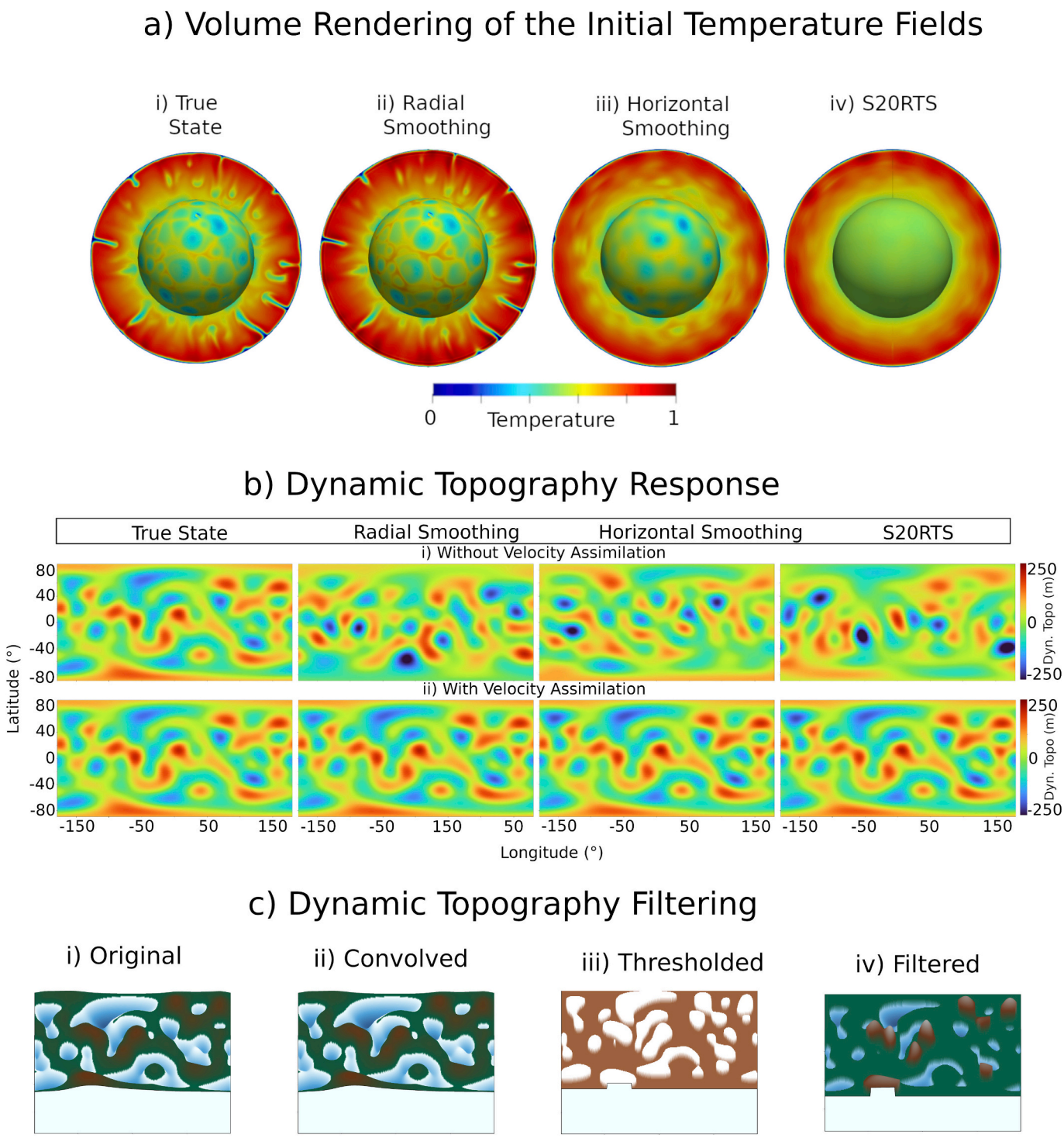

Fig. 1. a) Initial temperature field (blue = cold, red = hot) for a purely internally heated isoviscous mantle convection model (True State) together with perturbed states (Radial Smoothing, Horizontal Smoothing and S20RTS), see text. b) Dynamic topography response of the mantle models in (a) after one transit time, without/with assimilation of the horizontal component of the velocity field of the true state. c) Object identification workflow shown as an example for the true state dynamic topography field in (b). The field is first convolved (ii) with a disk of radius 20 gridpoints, then a threshold (iii) is set to remove weak regions after which the filtered field (iv) is obtained. Note that the convolution-thresholding procedure filters out weak uplift and subsidence areas while preserving significant dynamic topography. See Section 2 for details. (For interpretation of the references to colour in this figure legend, the reader is referred to the web version of this article.)

2. Methodology

We present an object-based method for comparing any number of dynamic topography fields. Following the twin experiment approach (Lorenz, 1965), we refer to the true state (see True State in Fig. 1b) as the observation/reference and the the other fields (see Radial Smoothing, Horizontal Smoothing and S20RTS in Fig. 1b) as predictions.

2.1. Object detection algorithm

Using the convolution-thresholding approach (Davis et al., 2006a), we identify distinct objects on both prediction and observation fields

Table 1
Summary of SAL scores for uplift and subsidence areas without/with velocity assimilation for the following cases: radial smoothing, horizontal smoothing and S20RTS. Note that SAL scores are farther/closer from/to 0 for cases without/with velocity assimilation.

	Uplift			Subsidence		
Case	Structure	Amplitude	Location	Structure	Amplitude	Location
Rad. Smoothing	−0.38/0.03	−0.14/0.04	0.18/0.02	−0.26/0.04	0.01/0.07	0.07/0.004
Hor. Smoothing	−0.38/0.07	−0.14/0.04	0.16/0.016	−1.30/−0.01	−0.20/0.11	0.12/0.06
S20RTS	0.56/0.07	−0.14/0.05	0.06/0.01	−0.77/−0.03	−0.11/0.11	0.25/0.07

and extract their statistics using scikit-image (van der Walt et al., 2014). It is necessary to move away from the mantle convection simulation grid onto a 1-degree grid for dynamic topography in order to apply the image processing tools. We first separate each field into its uplift and subsidence parts and extract objects in each part as follows: we apply a convolution filter to smooth the field and remove small-scale variations. The smoothing is performed by convolving the field with a disk (see Fig. 1c(ii)). This convolution replaces the data value at every gridpoint with the average of the data values at all other gridpoints contained within a disk centered at that gridpoint. In our case we employ a disk radius of 20 gridpoints for fields on a 1-degree grid resolution equivalent to a radius of 2000 km. A smaller radius leads to the identification of smaller objects and vice-versa. For global studies on structured grids, the grid values could be weighted by the cosine of the latitude of the associated grid point during convolution. Next, we threshold the smoothed field at every gridpoint to allow for the detection of object boundaries and to remove weak uplift/subsidence regions (see Fig. 1c(iii)). The value of our threshold for uplift and subsidence areas represents the average of the uplift and subsidence grid point values respectively and in this case is 120 m. In our case, this value captures the prominent dynamic topography objects that can also be detected by a human observer. The thresholded field results in a mask of 1s and 0s (with 1s at grid points beyond the threshold and 0s otherwise). This mask is then placed on the original field and results in local, isolated, patches of uplift and subsidence objects surrounded by regions of zero values (see Fig. 1c (iv)). Since we place the mask on the original field and not on the smoothed field, we retain the original topography values for later analyses. We then match prediction and observation objects. In order to overcome the double penalty problem (see Section 1), we remove the requirement for perfect overlap of prediction and observation objects. As such, a pair of objects is matched if they share $\geq 25\%$ of grid points and have an area ratio $(area_{min}/area_{max}) \geq 0.4$. These choices were found, in our case, to produce accurate matches.

2.2. Level 1: performance diagram

In constructing a performance diagram (Roebber, 2009), we define a hit, miss and false alarm. An object in the observation that is also present in the prediction is called a hit. An object in the observation that is not in the prediction is called a miss. Objects not in the observation but in the prediction are false alarms. We follow (Schaefer, 1990) and calculate the critical success index (CSI), probability of detection (POD), false alarm ratio (FAR), success ratio (SR) and bias as measures of prediction skill:

$$CSI = A/(A+B+C) \tag{2}$$

$$POD = A/(A+B) \tag{3}$$

$$FAR = C/(A+C) \tag{4}$$

$$SR = 1 - FAR \tag{5}$$

$$Bias = (A+C)/(A+B) \tag{6}$$

where A, B, C represent total hits, misses and false alarms respectively.

The CSI measures the ability of the prediction to produce objects that match observation objects. The POD is the proportion of objects that are correctly predicted in comparison to total observed objects while the FAR is a measure of the failure of the prediction to exclude the no-event/false cases. The bias is the degree of correspondence between the average prediction and the average observation. By exploiting the geometrical relationship between these measures, a performance diagram, connecting all measures, can be plotted. For accurate predictions, CSI, POD, SR and bias all approach 1, so that a perfect prediction lies at the upper right corner of the diagram (see Fig. 2a,b).

2.3. Level 2: SAL score

In order to compare object statistics without matching object pairs, we apply the Structure, Amplitude and Location (SAL) score (Wernli et al., 2008), originally introduced for the verification of precipitation forecasts. The structure (S) score compares the scaled dynamic topographies (i.e. scaled with respect to the maximum topography within an object) of all objects in the prediction with those in the observation. This score takes on large positive values if large, flat objects are predicted relative to the observation. Negative values of S arise if smaller, strongly peaked objects are predicted relative to the observation. The amplitude (A) score compares the average dynamic topography of the prediction with that of the observation and is a measure of the amplitude deviation of the prediction from the observation. This score takes on positive values if the prediction overestimates total topography while negative values indicate underestimation. The location (L) score is split into two components. The first component measures the distance between the centers of mass of the prediction and observation fields and the second component measures the averaged distance between the center of mass of the entire field and the centers of mass of the individual objects. The final location score is a sum of both scores.

We compute the structure score as follows. For every object, a scaled intensity is defined as

$$I_n = \sum_i T_i \Big/ T_n^{max} = T_n \Big/ T_n^{max} \tag{7}$$

where T_i is the topography value at gridpoint i within an object, n, and T_n^{max} represents the maximum/minimum topography for uplift/subsidence regions within the object. The scaled intensity is calculated separately for all objects in the observation and prediction after which the weighted mean of all objects' scaled intensity is determined:

$$I(T) = \frac{\sum_{n=1}^{M} T_n I_n}{\sum_{n=1}^{M} T_n} \tag{8}$$

where M represents the total number of identified objects.

Finally, the S score is defined as

$$S = \frac{I(T_{fcst}) - I(T_{obs})}{0.5\left[I(T_{fcst}) + I(T_{obs})\right]} \in [-2, 2] \tag{9}$$

where T_{fcst} and T_{obs} represent the forecast and observed dynamic topography respectively.

The amplitude score is calculated as the normalized topography difference between the observation and prediction averaged over the entire field, F:

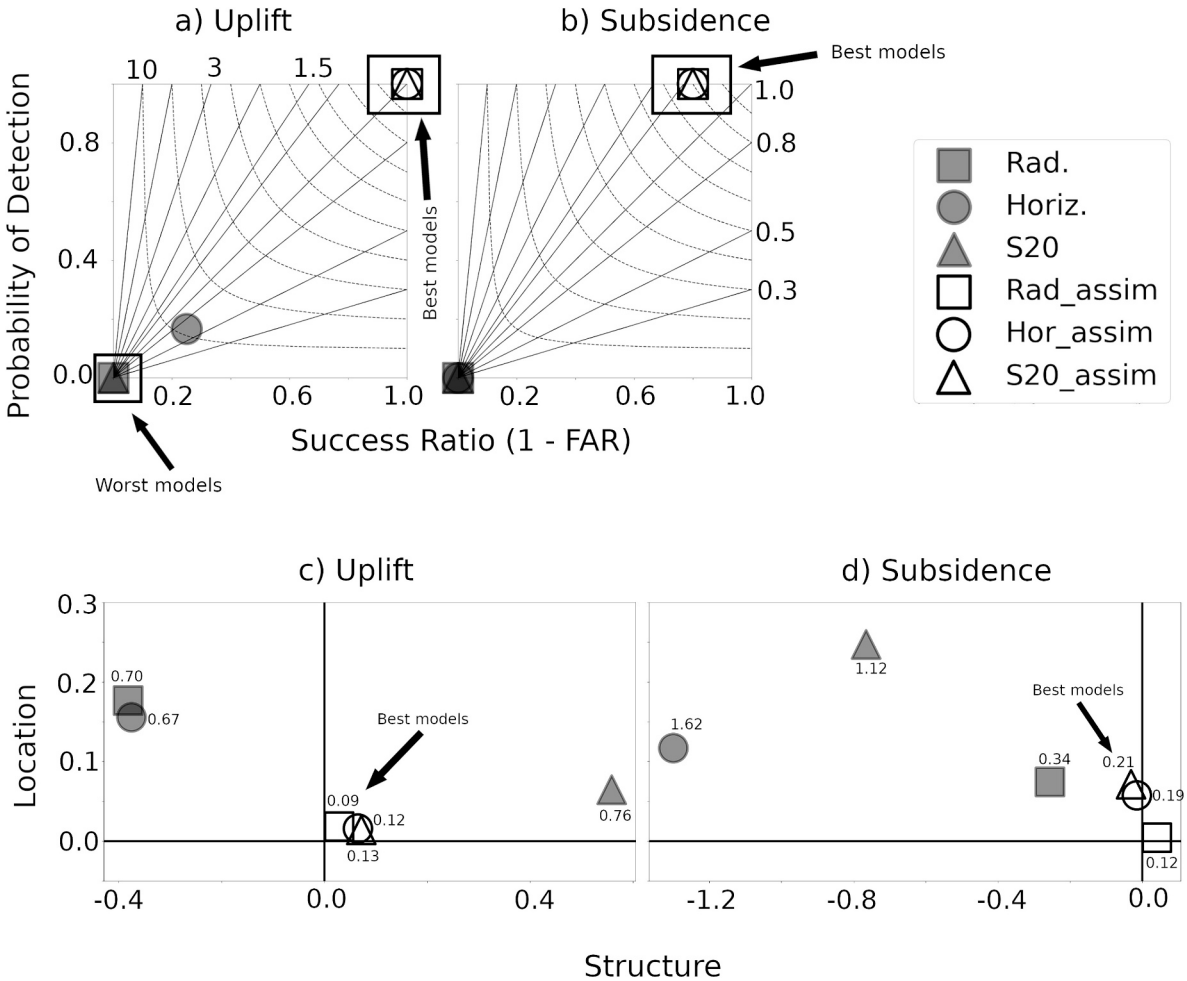

Fig. 2. Performance diagram and SAL scores (see Sections 2.2 and 2.3 respectively) between identified objects in the true state dynamic topography field and the perturbed cases (see Section 1.1 for detailed description of the various cases). Top panel (a)/(b): Performance Diagram for uplift/subsidence areas of dynamic topography. Vertical/horizontal axis denotes probability of detection/success ratio. Dotted contours represent Critical Success Index and outwardly extending solid lines represent bias scores. In both (a) and (b), figure markers plot on top of each other. Note that models with/without velocity assimilation lie close to the upper right/lower left corner, indicating good/poor similarity to the true state. Also note that the subsidence scores are slightly lower than the uplift scores. Bottom panel (c)/(d): Structure, Amplitude and Location (SAL) scores for the uplift/subsidence areas of dynamic topography. L/S scores are on the y/x axis. The amplitude (A) score is displayed adjacent to each marker on the plot. SAL scores close to 0 imply high similarity to the true state. Note that SAL scores are generally closer/farther to/from 0 for models with/without velocity assimilation. Also note that the subsidence scores are slightly higher than the uplift scores.

$$A = \frac{F(T_{fcst}) - F(T_{obs})}{0.5\left[F(T_{fcst}) + F(T_{obs})\right]} \in [-2, 2] \tag{10}$$

where $F(T)$, the field average of the topography field, T, is defined as:

$$F(T) = \frac{1}{N}\sum_{i \in F} T_i \tag{11}$$

where the T_i are the gridpoint values in the entire field and N represents the total number of gridpoints.

The first component of the location score measures the normalized distance between the centers of mass of the prediction and observation:

$$L_1 = \frac{\left|\mathbf{x}(T_{fcst}) - \mathbf{x}(T_{obs})\right|}{d} \in [0, 1] \tag{12}$$

where d is the largest distance between any two points in the field and $\mathbf{x}(T)$ is the center of mass of the entire topography field.

The second component considers the averaged distance between the centers of mass of the total topography field and individual objects. For each object we calculate the total topography within it as

$$T_n = \sum_i T_i \tag{13}$$

where the T_i are the gridpoint values in that object.

The weighted averaged distance between the centers of mass of the individual objects, $\mathbf{x}_n$, and the center of mass of the total topography field, $\mathbf{x}$, is then given by

$$r = \frac{\sum_{n=1}^{M} R_n \left|\mathbf{x} - \mathbf{x}_n\right|}{\sum_{n=1}^{M} R_n} \tag{14}$$

here R_n represents the total amount of topography contained within an object.

And the second location score is given as

$$L_2 = 2\left[\frac{\left|r(T_{fcst}) - r(T_{obs})\right|}{d}\right] \in [0, 1] \tag{15}$$

2.4. Level 3: Procrustes shape analysis

To compare matched object pairs, we apply a Procrustes analysis (Micheas et al., 2007; Lack et al., 2010). For every matched pair, we

attempt to fit, as close as possible, the geometry of the boundary of the prediction object to that of the observation. The object boundaries are extracted using a marching squares algorithm (Maple, 2003). Given matrices O and P which represent the latitude-longitude coordinates of the object boundaries of any matched pair of observation and prediction objects respectively, the Procrustes method finds an orthogonal transformation matrix Ω that closely maps P to O by minimizing a Frobenius norm as follows:

$$\begin{aligned} \underset{\Omega}{argmin}\left(\|O-\Omega P\|_F\right) &= \underset{\Omega}{argmin}\left(\|O-\Omega P\|_F^2\right) \\ &= \underset{\Omega}{argmin}\left(tr\left((O-\Omega P)^T(O-\Omega P)\right)\right) \\ &= \underset{\Omega}{argmin}\left(tr\left(O^TO+P^T\Omega^T\Omega P-2O^T\Omega P\right)\right) \\ &= \underset{\Omega}{argmin}\left(tr\left(O^TO\right)+tr\left(P^TP\right)-2tr\left(O^T\Omega P\right)\right) \\ &= \underset{\Omega}{argmax}\left(tr\left(O^T\Omega P\right)\right) \\ &= \underset{\Omega}{argmax}\left(tr\left(PO^T\Omega\right)\right) \\ &= \underset{\Omega}{argmax}\left(tr\left(\left(U\Sigma V^T\right)\Omega\right)\right) \\ &= \underset{\Omega}{argmax}\left(tr\left(\Sigma\left(V^T\Omega U\right)\right)\right) \\ &= VU^T \end{aligned} \tag{16}$$

subject to $\Omega^T\Omega = I$, where I is the identity matrix, U and V are the left and right singular vectors respectively and Σ is the singular value matrix after a singular value decomposition of PO^T.

Apart from the transformed matrix ΩP, the procedure also outputs the sum of squared errors (SSE) between matrices O and ΩP normalized between 0 (best score) and 1 (worst score). We also compute the difference in average topography for each matched object pair and normalize this value between 0 (best score) and 1 (worst score). This normalized difference is denoted as θ. The preliminary score per matched object pair is given as

$$S_{prel} = SSE + \theta \tag{17}$$

such that for a perfect match, $S_{prel} = 0$ and for no match, $S_{prel} = 2$. For K matched object pairs, the average preliminary score is given by

$$S_{prel_{ave}} = \frac{\sum_{i=1}^{K} S_{prel_i}}{K} \tag{18}$$

The final score combines $S_{prel_{ave}}$ with the CSI defined in Section 2.2:

$$S_{total} = S_{prel_{ave}} + (1 - CSI) \tag{19}$$

The inclusion of the CSI helps to penalize predictions that produce few object matches with the observation even if these matches are highly accurate. In the case where there are no matches between the prediction and observation objects, CSI = 0 and $S_{prel_{ave}}$ is simply a sum of the worst SSE and θ scores. The final score then becomes

$$S_{total} = 1 + 1 + 1 = 3 \tag{20}$$

3. Results

3.1. Performance diagram

The Performance Diagrams for uplift and subsidence areas are shown in Fig. 2a/b. For uplift regions (Fig. 2a) the models have the following scores without/with velocity assimilation: radial smoothing has POD = 0/1, SR = 0/1, CSI = 0/1. Horizontal smoothing has POD = 0.18/1, SR = 0.22/1 and CSI = 0.1/1. S20RTS has POD = 0/1, SR = 0/1 and CSI = 0/1. For subsidence regions (Fig. 2b), radial, horizontal and S20RTS smoothing all have POD = 0/1, SR = 0/0.8 and CSI = 0/0.8.

3.2. SAL score

Fig. 2c/d show the SAL scores for uplift and subsidence regions. In the uplift regions (Fig. 2c) the scores are as follows without/with velocity assimilation: radial smoothing has S = −0.38/0.03, A = −0.14/0.04 and L = 0.18/0.02. Horizontal smoothing has S = −0.38/0.07, A = −0.14/0.04 and L = 0.16/0.016. S20RTS has S = 0.56/0.07, A = −0.14/0.05 and L = 0.06/0.01. For the subsidence regions (Fig. 2d), the scores are as follows without/with velocity assimilation: radial smoothing has S = −0.26/0.04, A = 0.01/0.07 and L = 0.07/0.004. Horizontal smoothing has S = −1.30/−0.01, A = −0.20/0.11 and L = 0.12/0.06. S20RTS has S = −0.77/−0.03, A = −0.11/0.11 and L = 0.25/0.07. To consolidate the SAL score into a single number, we sum the absolute values of S, A and L and obtain a combined SAL score. Fig. 3a shows the combined SAL score for uplift and subsidence areas across all models. For cases without/with velocity assimilation, we have the following scores for uplift areas: radial smoothing (0.70/0.09), horizontal smoothing (0.67/0.12), S20RTS (0.76/0.13). For the subsidence regions, the scores without/with velocity assimilation are: radial smoothing (0.34/0.12), horizontal smoothing (1.62/0.19), S20RTS (1.12/0.21).(Fig. 4)

3.3. Procrustes score

The Procrustes skill score for all models is shown in Fig. 3b. The scores are as follows without/with velocity assimilation: radial smoothing has an uplift score of 3/0.76 and a subsidence score of 3/1.30. Horizontal smoothing has an uplift score of 1.96/0.66 and a subsidence score of 3/1.31 while S20RTS has an uplift score of 3/0.70 and a subsidence score of 3/1.27.

4. Discussion and conclusion

In assessing mantle flow trajectories, it is attractive to use dynamic topography predictions as a proxy. This is because mantle flow, as expressed in terms of time-dependent fields, cannot be directly observed but must be inferred via its surface effects. Using an object-based approach, we here verify earlier results (Colli et al., 2015; Vynnytska and Bunge, 2015; Bocher et al., 2016; Bocher et al., 2018) on the efficacy of velocity assimilation in minimizing the butterfly effect. Our assessment of mantle flow trajectories via their dynamic topography predictions shows that models with velocity assimilation outperform those without (see Figs. 2a-d, 3a and b). The object-based approach allows us to probe the properties of identified dynamic topography objects. For instance, Fig. 2a,b show that models with velocity assimilation predict dynamic topography objects that match those in the reference twin. Furthermore, they show the difference between uplift and subsidence areas of dynamic topography. One sees in both figures that uplift areas are better predicted (as evidenced by all models lying on the upper right corner) than subsidence areas (as seen by the models lying slightly to the left of the upper right corner). This is superior to traditional assessment approaches such as correlation, which hide a great deal of model information behind a single number. The ability of our approach to separate the dynamic topography field into its uplift and subsidence regions makes it appropriate for comparisons with geological observations. Subsidence areas of dynamic topography are well constrained via past shorelines (Smith et al., 2004) while uplift areas are coming into focus via hiatus mapping (Friedrich et al., 2018; Vibe et al., 2018; Carena et al., 2019). Moreover, the object-based approach allows one to focus on specific regions of interest. A next step could involve the application of this approach to geological and geophysical indicators of past and current dynamic topography. We note that the methods introduced here do not depend on the specific geometry or pattern of the field under investigation, so that they can be applied to real dynamic topography inferences (e.g. Hoggard et al., 2021; Davies et al., 2022).

In extracting objects from the dynamic topography field, our

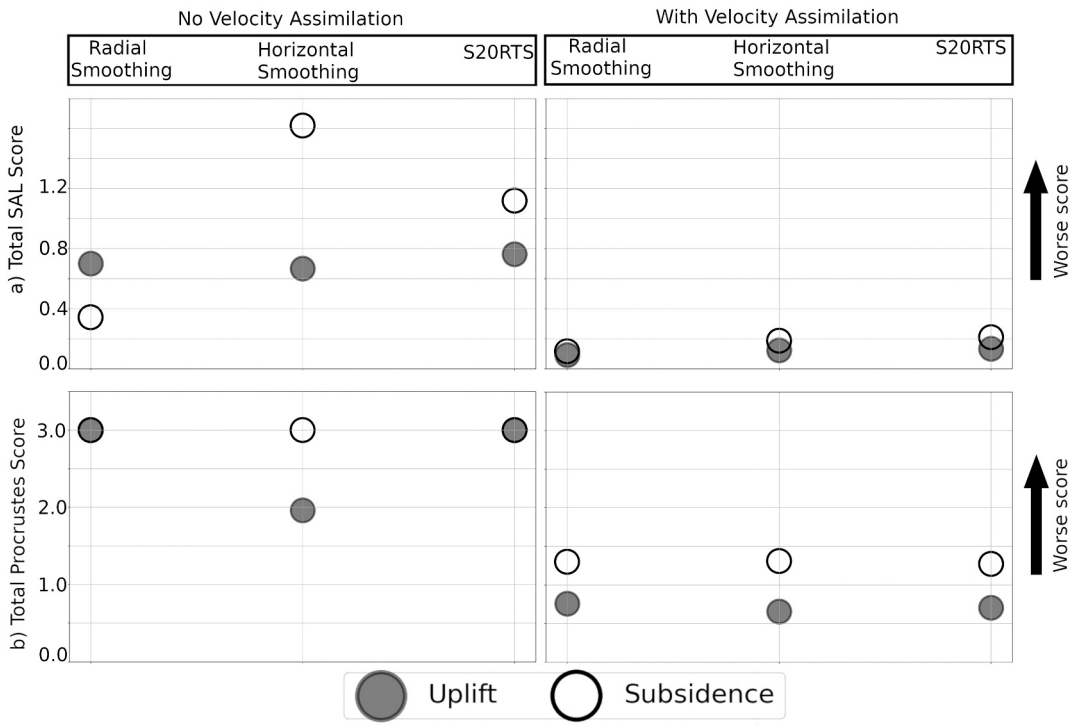

Fig. 3. Total structure, amplitude and location (SAL) (top panel) and Procrustes scores (bottom panel) for uplift (filled circle) and subsidence (unfilled circle) areas of dynamic topography with and without velocity assimilation, see text. Scores are calculated between the true state dynamic topography field and perturbed cases respectively (see Section 1.1 for detailed description of the various cases). Also see Sections 2.3 and 2.4 for details on SAL and Procrustes scores respectively. Note that the total SAL and Procrustes scores for uplift and subsidence regions are lower/higher with/without the assimilation of the horizontal component of the surface velocity field of the true state implying good/poor similarity to the true state.

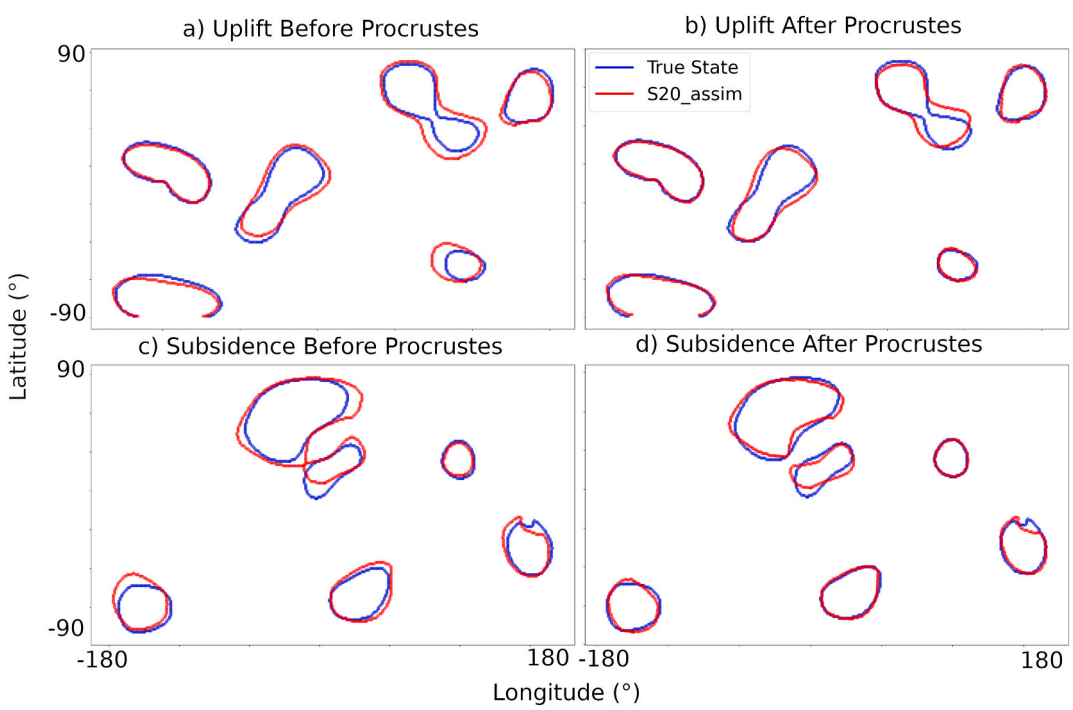

Fig. 4. Procrustes shape fitting of the boundaries of matched objects in the reference dynamic topography field (see True State in Fig. 1b) shown in blue and the tomographically-filtered S20RTS field with velocity assimilation (see S20RTS in lower row of Fig. 1b) shown in red. Plots are shown separately for uplift and subsidence regions. (a)/(c) Uplift/subsidence boundaries before Procrustes fitting. (b)/(d) Uplift/subsidence boundaries after Procrustes fitting. Note that the boundaries of the S20RTS objects are displaced from those in the reference field before Procrustes fitting. After fitting, however, object boundaries better align. (For interpretation of the references to colour in this figure legend, the reader is referred to the web version of this article.)

convolution radius of 2000 km was chosen to represent the size of hiatus surfaces on a continental scale (Hayek et al., 2020; Hayek et al., 2021). We also chose to match objects between fields if they shared at least 25% of gridpoints. This was a subjective choice which, in our case, produced realistic matches between fields. A potential limitation of this choice is that multiple objects in the forecast field could be matched to the same object in the observed field. In this case, other objective criteria (e.g. Davis et al., 2006a; Davis et al., 2006b) could be applied in future work. Such criteria could consider matching as a function of the distance between the centroids of identified objects. An example approach is to match objects only if the distance between their centroids is less than the sum of the sizes of both objects. In the case of multiple overlaps, the procedure selects the overlap that has the smallest distance in comparison to the object sizes. Another limitation is that real dynamic topography fields are often sparse and non-uniform (in space and time), thus hindering our ability to apply the methods described in this paper. One possible approach to overcome this limitation is the use of geospatial interpolation techniques whereby the values at poorly sampled locations are estimated by weighted linear combinations of the values at nearby locations. Such methods are referred to as kriging (Hohn, 1991) and could be brought to bear in the case of dynamic topography. Care should also be shown in the selection of threshold values in order to prevent the misidentification of objects. In this work, we used a threshold of 120 m, representative of the average dynamic topography of uplift and subsidence areas respectively. This led to the generation of a false alarm for the subsidence areas as seen in Fig. 2b, where the models with velocity assimilation have a Success Ratio of 0.8. This false alarm then entered into the calculation of the SAL and Procrustes scores, thus explaining why uplift areas outperform subsidence areas even with velocity assimilation. For comparisons of real dynamic topography fields, the choice of threshold should be based on geologically relevant criteria.

Apart from the approaches introduced here, another verification method, known as optical flow (Keil and Craig, 2007; Keil and Craig, 2009), has been developed in meteorology to compare precipitation patterns and this can be considered for dynamic topography. Additionally, shape comparison approaches such as optimal mass transport (Monge, 1781; Villani, 2003; Villani, 2008) can be applied to compare the boundaries of uplift and subsidence areas on dynamic topography maps. The latter has been newly applied in seismology to compare synthetic seismograms against observed data (Sambridge et al., 2022). It is clear that these object-oriented/optical flow methods are well-suited to link the growing body of geological and geophysical observations to geodynamic models. For instance, the study of heat flux patterns may benefit from the object-based approach presented within this paper, since like the dynamic topography field, it is also, in essence, representable on a 2-D grid over the Earth surface.

5. Open research

The data used in this study were generated via numerical simulations by the authors as described in Section 1.1. We have used Paraview (Ahrens et al., 2005), Matplotlib (Hunter, 2007) and PyGMT (Uieda et al., 2022) for visualizations. Additionally, all codes written as part of this work can be provided upon request.

Author statement

Ayodeji Taiwo reports financial support was provided by German Academic Exchange Service. Ayodeji Taiwo reports financial support was provided by German Research Foundation. If there are other authors, they declare that they have no known competing financial interests or personal relationships that could have appeared to influence the work reported in this paper.

CRediT authorship contribution statement

Ayodeji Taiwo: Writing – original draft, Visualization, Validation, Software, Methodology, Investigation, Funding acquisition, Formal analysis, Conceptualization. **H.-P. Bunge:** Writing – review & editing, Validation, Supervision, Resources, Project administration, Funding acquisition, Conceptualization. **G. Craig:** Methodology, Conceptualization.

Declaration of competing interest

The authors declare that they have no known competing financial interests or personal relationships that could have appeared to influence the work reported in this paper.

Data availability

Data will be made available on request.

Acknowledgments

A. Taiwo thanks the Deutscher Akademischer Austausch Dienst (DAAD) and the German Science Foundation (DFG) for funding.

References

Ahrens, J., Geveci, B., Law, C., 2005. 36 - paraview: an end-user tool for large-data visualization. In: Hansen, C.D., Johnson, C.R. (Eds.), Visualization Handbook. Butterworth-Heinemann, Burlington, pp. 717–731. https://doi.org/10.1016/B978-012387582-2/50038-1. URL. https://www.sciencedirect.com/science/article/pii/B9780123875822500381.

Anthes, R.A., 1983. Regional models of the atmosphere in middle latitudes. Mon. Weather Rev. 6, 1306–1335. https://doi.org/10.1175/1520-0493(1983)111<1306:RMOTAI>2.0.CO;2. URL. https://journals.ametsoc.org/view/journals/mwre/111/6/1520-0493_1983_111_1306_rmotai_2_0_co_2.xml.

Baldwin, M.E., Kain, J.S., 2006. Sensitivity of several performance measures to displacement error, bias, and event frequency. Weather Forecast. 21 (4), 636–648.

Bello, L., Coltice, N., Tackley, P.J., Dietmar Müller, R., Cannon, J., 2015. Assessing the role of slab rheology in coupled plate-mantle convection models. Earth Planet. Sci. Lett. 430, 191–201. https://doi.org/10.1016/j.epsl.2015.08.010.

Bocher, M., Coltice, N., Fournier, A., Tackley, P., 2016. A sequential data assimilation approach for the joint reconstruction of mantle convection and surface tectonics. Geophys. J. Int. 204, 200–214. https://doi.org/10.1093/gji/ggv427.

Bocher, M., Fournier, A., Coltice, N., 2018. Ensemble Kalman filter for the reconstruction of the Earth's mantle circulation. Nonlinear Process. Geophys. 1, 99–123. https://doi.org/10.5194/npg-25-99-2018.

Braun, J., 2010. The many surface expressions of mantle dynamics. Nat. Geosci. 3 (12), 825–833. https://doi.org/10.1038/ngeo1020.

Bunge, H.P., Glasmacher, U.A., 2018. Models and observations of vertical motion (MoveOn) associated with rifting to passive margins: preface. Gondwana Res. 53, 1–8 rifting to Passive Margins. https://doi.org/10.1016/j.gr.2017.07.005. URL. https://www.sciencedirect.com/science/article/pii/S1342937X17302605.

Bunge, H.-P., Richards, M.A., Baumgardner, J.R., 2002. Mantle-circulation models with sequential data assimilation: inferring present-day mantle structure from plate-motion histories. Philos. Trans. Math. Phys. Eng. Sci. 360 (1800), 2545–2567. URL. http://www.jstor.org/stable/3558910.

Bunge, H.-P., Hagelberg, C.R., Travis, B.J., 2003. Mantle circulation models with variational data assimilation: inferring past mantle flow and structure from plate motion histories and seismic tomography. Geophys. J. Int. 152 (2), 280–301. https://doi.org/10.1046/j.1365-246X.2003.01823.x.

Carena, S., Bunge, H.-P., Friedrich, A.M., 2019. Analysis of geological hiatus surfaces across Africa in the Cenozoic and implications for the timescales of convectively-maintained topography. Can. J. Earth Sci. 56 (12), 1333–1346. https://doi.org/10.1139/cjes-2018-0329.

Casati, B., Wilson, L., Stephenson, D., Nurmi, P., Ghelli, A., Pocernich, M., Damrath, U., Ebert, E., Brown, B., Mason, S., 2008. Forecast verification: current status and future directions. Meteorol. Appl. 15 (1), 3–18.

Case, J.L., Manobianco, J., Lane, J.E., Immer, C.D., Merceret, F.J., 2004. An Objective Technique for Verifying Sea Breezes in High-Resolution Numerical Weather Prediction Models.

Colli, L., Bunge, H.-P., Schuberth, B.S.A., 2015. On retrodictions of global mantle flow with assimilated surface velocities. Geophys. Res. Lett. 42 https://doi.org/10.1002/2015GL066001.

Colli, L., Ghelichkhan, S., Bunge, H.-P., Oeser, J., 2018. Retrodictions of mid paleogene mantle flow and dynamic topography in the atlantic region from compressible high resolution adjoint mantle convection models: sensitivity to deep mantle viscosity and tomographic input model. Gondwana Res. 53, 252–272 rifting to Passive Margins.

https://doi.org/10.1016/j.gr.2017.04.027. URL. https://www.sciencedirect.com/science/article/pii/S1342937X17302125.
Davies, D.R, Ghelichkhan, S., Hoggard, M.J., Valentine, A.P., Richards, F.D., 2022. Observations and models of dynamic topography: current status and future directions. In: Dynamics of Plate Tectonics and Mantle Convection, pp. 223–269.
Davies, D.R., Valentine, A.P., Kramer, S.C., Rawlinson, N., Hoggard, M.J., Eakin, C.M., Wilson, C.R., 2019. Earth's multi-scale topographic response to global mantle flow. Nat. Geosci. 12.
Davis, C., Brown, B., Bullock, R., 2006a. Object-based verification of precipitation forecasts. Part I: methodology and application to mesoscale rain areas. Mon. Weather Rev. 134 (7), 1772. https://doi.org/10.1175/MWR3145.1.
Davis, C., Brown, B., Bullock, R., 2006b. Object-based verification of precipitation forecasts. Part II: application to convective rain systems. Mon. Weather Rev. 134 (7), 1785. https://doi.org/10.1175/MWR3146.1.
Davis, C., Brown, B.G., Bullock, R., Halley-Gotway, J., 2009. The method for object-based diagnostic evaluation (MODE) applied to numerical forecasts from the 2005 NSSL/SPC spring program. Weather Forecast. 24 (5), 1252. https://doi.org/10.1175/2009WAF2222241.1.
Flament, N., Gurnis, M., Müller, R.D., 2013. A review of observations and models of dynamic topography. Lithosphere 5 (2), 189–210. https://doi.org/10.1130/L245.1 arXiv: https://pubs.geoscienceworld.org/gsa/lithosphere/article-pdf/5/2/189/3039172/189.pdf.
Forte, A.M., Rowley, D.B., 2022. Earth's isostatic and dynamic topography—a critical perspective. Geochem. Geophys. Geosyst. 23 (9) https://doi.org/10.1029/2021GC009740 e2021GC009740.
Fowle, M.A., Roebber, P.J., 2003. Short-Range (0–48 h) Numerical Prediction of Convective Occurrence, Mode, and Location.
French, S.W., Romanowicz, B.A., 2014. Whole-mantle radially anisotropic shear velocity structure from spectral-element waveform tomography. Geophys. J. Int. 199 (3), 1303–1327. https://doi.org/10.1093/gji/ggu334 arXiv: https://academic.oup.com/gji/article-pdf/199/3/1303/5986895/ggu334.pdf.
Friedrich, A.M., Bunge, H.-P., Rieger, S.M., Colli, L., Ghelichkhan, S., Nerlich, R., 2018. Stratigraphic framework for the plume mode of mantle convection and the analysis of interregional unconformities on geological maps. Gondwana Res. 159–188. Rifting to Passive Margins. https://doi.org/10.1016/j.gr.2017.06.003.
Ghelichkhan, S., Bunge, H.-P., 2016. The compressible adjoint equations in geodynamics: derivation and numerical assessment. Int. J. Geomath. https://doi.org/10.1007/s13137-016-0080-5.
Ghelichkhan, S., Bunge, H.-P., Oeser, J., 2021. Global mantle flow retrodictions for the early Cenozoic using an adjoint method: evolving dynamic topographies, deep mantle structures, flow trajectories and sublithospheric stresses. Geophys. J. Int. 226 (2), 1432–1460. https://doi.org/10.1093/gji/ggab108 arXiv: https://academic.oup.com/gji/article-pdf/226/2/1432/38711003/ggab108.pdf.
Gilleland, E., Ahijevych, D., Brown, B.G., Casati, B., Ebert, E.E., 2009. Intercomparison of spatial forecast verification methods. Weather Forecast. 24 (5), 1416–1430.
Hager, B.H., Clayton, R.W., Richards, M.A., Comer, R.P., Dziewonski, A.M., 1985. Lower mantle heterogeneity, dynamic topography and the geoid. Nature 313.
Hayek, N., Vilacis, B., Bunge, H.-P., Friedrich, A., Carena, S., Vibe, Y., 2020. Continent-scale hiatus maps for the Atlantic realm and Australia since the Upper Jurassic and links to mantle flow induced dynamic topography. Proc. R. Soc. A. https://doi.org/10.1098/rspa.2020.0390.
Hayek, J.N., Vilacís, B., Bunge, H.-P., Friedrich, A.M., Carena, S., Vibe, Y., 2021. Correction: continent-scale hiatus maps for the Atlantic realm and Australia since the upper jurassic and links to mantle flow-induced dynamic topography. Proc. R. Soc. A 477 (2251), 20210437. https://doi.org/10.1098/rspa.2021.0437.
Hoggard, M.J., White, N., Al-Attar, D., 2016. Global dynamic topography observations reveal limited influence of large-scale mantle flow. Nat. Geosci. 9.
Hoggard, M., Austermann, J., Randel, C., Stephenson, S., 2021. Observational estimates of dynamic topography through space and time. In: Mantle Convection and Surface Expressions, pp. 371–411.
Hohn, M.E., 1991. An introduction to applied geostatistics: by edward H. Isaaks and R. Mohan Srivastava, 1989, Oxford University Press, New York, 561 p., isbn 0-19-505012-6, isbn 0-19-505013-4 (paperback), 55.00*cloth*, 35.00 paper (us). Comput. Geosci. 17 (3), 471–473. https://doi.org/10.1016/0098-3004(91)90055-I. https://www.sciencedirect.com/science/article/pii/009830049190055I.
Holdt, M.C., White, N.J., Stephenson, S.N., Conway-Jones, B.W., 2022. Densely sampled global dynamic topographic observations and their significance. J. Geophys. Res. Solid Earth 127 (7). https://doi.org/10.1029/2022JB024391 e2022JB024391.
Horbach, A., Bunge, H.-P., Oeser, J., 2014. The adjoint method in geodynamics: derivation from a general operator formulation and application to the initial condition problem in a high resolution mantle circulation model. GEM - Int. J. Geomath. 5 (2), 163–194. https://doi.org/10.1007/s13137-014-0061-5.
Hunter, J.D., 2007. Matplotlib: a 2d graphics environment. Comput. Sci. Eng. 9 (3), 90–95. https://doi.org/10.1109/MCSE.2007.55.
Ismail-Zadeh, A., Schubert, G., Tsepelev, I., Korotkii, A., 2004. Inverse problem of thermal convection: numerical approach and application to mantle plume restoration. Phys. Earth Planet. Inter. 145 (1), 99–114. https://doi.org/10.1016/j.pepi.2004.03.006. URL. http://www.sciencedirect.com/science/article/pii/S0031920104001384.
Jolliffe, I.T., Stephenson, D.B., 2012. Forecast Verification: A practitioner's Guide in Atmospheric Science. John Wiley & Sons.
Keil, C., Craig, G., 2007. A displacement-based error measure applied in a regional ensemble forecasting system. Mon. Weather Rev. 135, 3248–3259. https://doi.org/10.1175/MWR3457.1.
Keil, C., Craig, G., 2009. A displacement and amplitude score employing an optical flow technique. Weather Forecast. 24, 1297–1308.
Lack, S.A., Limpert, G.L., Fox, N.I., 2010. An object-oriented multiscale verification scheme. Weather Forecast. 25 (1), 79–92. https://doi.org/10.1175/2009WAF2222245.1. URL. https://journals.ametsoc.org/view/journals/wefo/25/1/2009waf2222245_1.xml.
Lithgow-Bertelloni, C., Silver, P.G., 1998. Dynamic topography, plate driving forces and the African superswell. Nature 395, 269–272. https://doi.org/10.1038/26212.
Lorenz, E.N., 1965. A study of the predictability of a 28-variable atmospheric model. Tellus 17 (3), 321–333. https://doi.org/10.1111/j.2153-3490.1965.tb01424.x.
Maple, C., 2003. Geometric design and space planning using the marching squares and marching cube algorithms. In: 2003 International Conference on Geometric Modeling and Graphics, 2003. Proceedings, pp. 90–95. https://doi.org/10.1109/GMAG.2003.1219671.
Mass, C.F., Ovens, D., Westrick, K., Colle, B.A., 2002. Does increasing horizontal resolution produce more skillful forecasts? Bull. Am. Meteorol. Soc. 83 (3), 407–430. https://doi.org/10.1175/1520-0477(2002)083<0407:DIHRPM>2.3.CO;2.
McNamara, A.K., Zhong, S., 2005. Degree-one mantle convection: dependence on internal heating and temperature-dependent rheology. Geophys. Res. Lett. 32 (1) https://doi.org/10.1029/2004GL021082.
Micheas, A., Fox, N.I., Lack, S.A., Wikle, C.K., 2007. Cell Identification and Verification of qpf Ensembles using Shape Analysis Techniques, 344, pp. 105–116.
Monge, G., 1781. Mémoire sur la théorie des déblais et des remblais. In: Histoire de l'Académie Royale des Sciences de Paris.
Müller, R.D., Seton, M., Zahirovic, S., Williams, S.E., Matthews, K.J., Wright, N.M., Shephard, G.E., Maloney, K.T., Barnett-Moore, N., Hosseinpour, M., Bower, D.J., Cannon, J., 2016. Ocean Basin evolution and global-scale plate reorganization events since Pangea breakup. Annu. Rev. Earth Planet. Sci. 44 (1), 107–138. https://doi.org/10.1146/annurev-earth-060115-012211.
Müller, R.D., Flament, N., Cannon, J., Tetley, M.G., Williams, S.E., Cao, X., Bodur, O.F., Zahirovic, S., Merdith, A., 2022. A tectonic-rules-based mantle reference frame since 1 billion years ago – implications for supercontinent cycles and plate–mantle system evolution. Solid Earth 13 (7), 1127–1159. https://doi.org/10.5194/se-13-1127-2022. URL. https://se.copernicus.org/articles/13/1127/2022/.
Price, M.G., Davies, J.H., 2017. Profiling the robustness, efficiency and limits of the forward-adjoint method for 3-D mantle convection modelling. Geophys. J. Int. 212 (2), 1450–1462. https://doi.org/10.1093/gji/ggx489 arXiv: https://academic.oup.com/gji/article-pdf/212/2/1450/22793118/ggx489.pdf.
Richards, M.A., Hager, B.H., 1984. Geoid anomalies in a dynamic Earth. J. Geophys. Res. Solid Earth 89 (B7), 5987–6002. https://doi.org/10.1029/JB089iB07p05987.
Richards, F.D., Hoggard, M.J., White, N., Ghelichkhan, S., 2020. Quantifying the relationship between short-wavelength dynamic topography and thermomechanical structure of the upper mantle using calibrated parameterization of anelasticity. J. Geophys. Res. Solid Earth 125 (9). https://doi.org/10.1029/2019JB019062 e2019JB019062.
Ritsema, J., van Heijst, H.J., Woodhouse, J.H., 2004. Global transition zone tomography. J. Geophys. Res. Solid Earth 109 (B2). https://doi.org/10.1029/2003JB002610.
Ritsema, J., Deuss, H.V.H.A., Woodhouse, J., 2011. S40RTS: a degree-40 shear-velocity model for the mantle from new Rayleigh wave dispersion, teleseismic traveltime and normal-mode splitting function measurements. Geophys. J. Int. 184, 1223–1236.
Roberts, G.G., White, N., 2010. Estimating uplift rate histories from river profiles using African examples. J. Geophys. Res. Solid Earth 115 (B2). https://doi.org/10.1029/2009JB006692.
Roebber, P.J., 2009. Visualizing multiple measures of forecast quality. Weather Forecast. 2, 601–608. https://doi.org/10.1175/2008WAF2222159.1.
Sambridge, M., Jackson, A., Valentine, A.P., 2022. Geophysical inversion and optimal transport. Geophys. J. Int. https://doi.org/10.1093/gji/ggac151 arXiv: https://academic.oup.com/gji/advance-article-pdf/doi/10.1093/gji/ggac151/43409539/ggac151.pdf.
Schaefer, J.T., 1990. The critical success index as an indicator of warning skill. Weather Forecast. 5 (4), 570–575. https://doi.org/10.1175/1520-0434(1990)005<0570:TCSIAA>2.0.CO;2. URL. https://journals.ametsoc.org/view/journals/wefo/5/4/1520-0434_1990_005_0570_tcsiaa_2_0_co_2.xml.
Schuberth, B.S.A., Bunge, H.-P., Steinle-Neumann, G., Moder, C., Oeser, J., 2009. Thermal versus elastic heterogeneity in high-resolution mantle circulation models with pyrolite composition: high plume excess temperatures in the lowermost mantle. Geochem. Geophys. Geosyst. 10 (1) https://doi.org/10.1029/2008GC002235.
Şengör, A.M.C., 2001. Elevation as indicator of mantle-plume activity. In: Mantle Plumes: Their Identification Through Time. Geological Society of America. https://doi.org/10.1130/0-8137-2352-3.183.
Shephard, G., Bunge, H.-P., Schuberth, B., Müller, R., Talsma, A., Moder, C., Landgrebe, T., 2012. Testing absolute plate reference frames and the implications for the generation of geodynamic mantle heterogeneity structure. Earth Planet. Sci. Lett. 317-318, 204–217. https://doi.org/10.1016/j.epsl.2011.11.027. URL. https://www.sciencedirect.com/science/article/pii/S0012821X11006844.
Simmons, N., Forte, A., Grand, S., 2007. Thermochemical structure and dynamics of the African superplume. Geophys. Res. Lett. 34 (2).
Smith, B.B., Mullen, S.L., 1993. An Evaluation of Sea Level Cyclone Forecasts Produced by nmc's Nested-Grid Model and Global Spectral Model.
Smith, A.G., Smith, D.G., Funnell, B.M., 2004. Atlas of Mesozoic and Cenozoic Coastlines.
Stewart, C.A., Turcotte, D.L., 1989. The route to chaos in thermal convection at infinite Prandtl number: 1. Some trajectories and bifurcations. J. Geophys. Res. Solid Earth 94 (B10), 13707–13717. https://doi.org/10.1029/JB094iB10p13707.
Taiwo, A., Bunge, H.-P., Schuberth, B.S.A., Colli, L., Vilacis, B., 2023. Robust global mantle flow trajectories and their validation via dynamic topography histories. Geophys. J. Int. https://doi.org/10.1093/gji/ggad188.

Trampert, J., Spetzler, J., 2006. FAST TRACK PAPER: surface wave tomography: finite-frequency effects lost in the null space. Geophys. J. Int. 164, 394–400. https://doi.org/10.1111/j.1365-246X.2006.02864.x.

Uieda, L., Tian, D., Leong, W.J., Jones, M., Schlitzer, W., Grund, M., Toney, L., Fröhlich, Y., Yao, J., Magen, Y., Materna, K., Belem, A., Newton, T., Anant, A., Ziebarth, M., Quinn, J., Wessel, P., Dec. 2022. PyGMT: A Python Interface for the Generic Mapping Tools. https://doi.org/10.5281/zenodo.7481934.

Valentine, A.P., Davies, D.R., 2020. Global models from sparse data: a robust estimate of Earth's residual topography spectrum. Geochem. Geophys. Geosyst. 21 (8) https://doi.org/10.1029/2020GC009240 e2020GC009240.

van der Walt, S., Schönberger, J.L., Nunez-Iglesias, J., Boulogne, F., Warner, J.D., Yager, N., Gouillart, E., Yu, T., the scikit-image contributors, 2014. Scikit-image: image processing in Python. PeerJ 2, e453. https://doi.org/10.7717/peerj.453.

Vibe, Y., Friedrich, A., Bunge, H.-P., Clark, S., 2018. Correlations of oceanic spreading rates and hiatus surface area in the North Atlantic realm. Lithosphere 10 (5), 677–684. https://doi.org/10.1130/L736.1 arXiv: https://pubs.geoscienceworld.org/gsa/lithosphere/article-pdf/10/5/677/4344179/677.pdf.

Villani, C., 2003. Topics in Optimal Transportation, Graduate Studies in Mathematics, vol. v. 58. American Mathematical Society, Providence, R.I.

Villani, C., 2008. Optimal transport, old and new. Notes for the 2005 saint-flour summer school. In: Grundlehren der Mathematischen Wissenschaften [Fundamental Principles of Mathematical Sciences]. Springer.

Vynnytska, L., Bunge, H., 2015. Restoring past mantle convection structure through fluid dynamic inverse theory: regularisation through surface velocity boundary conditions. Int. J. Geomath. 6 https://doi.org/10.1007/s13137-014-0060-6.

Wernli, H., Paulat, M., Hagen, M., Frei, C., 2008. Sal—a novel quality measure for the verification of quantitative precipitation forecasts. Mon. Weather Rev. 136 (11), 4470–4487. https://doi.org/10.1175/2008MWR2415.1. URL. https://journals.ametsoc.org/view/journals/mwre/136/11/2008mwr2415.1.xml.

Wilks, D.S., 2011. Statistical Methods in the Atmospheric Sciences, vol. 100. Academic press.